Development and application of a volume penalization immersed boundary method for the computation of blood flow and shear stresses in cerebral vessels and aneurysms

Julia Mikhal & Bernard J. Geurts

Journal of Mathematical Biology

ISSN 0303-6812
Volume 67
Combined 6-7

J. Math. Biol. (2014) 67:1847-1875
DOI 10.1007/s00285-012-0627-5

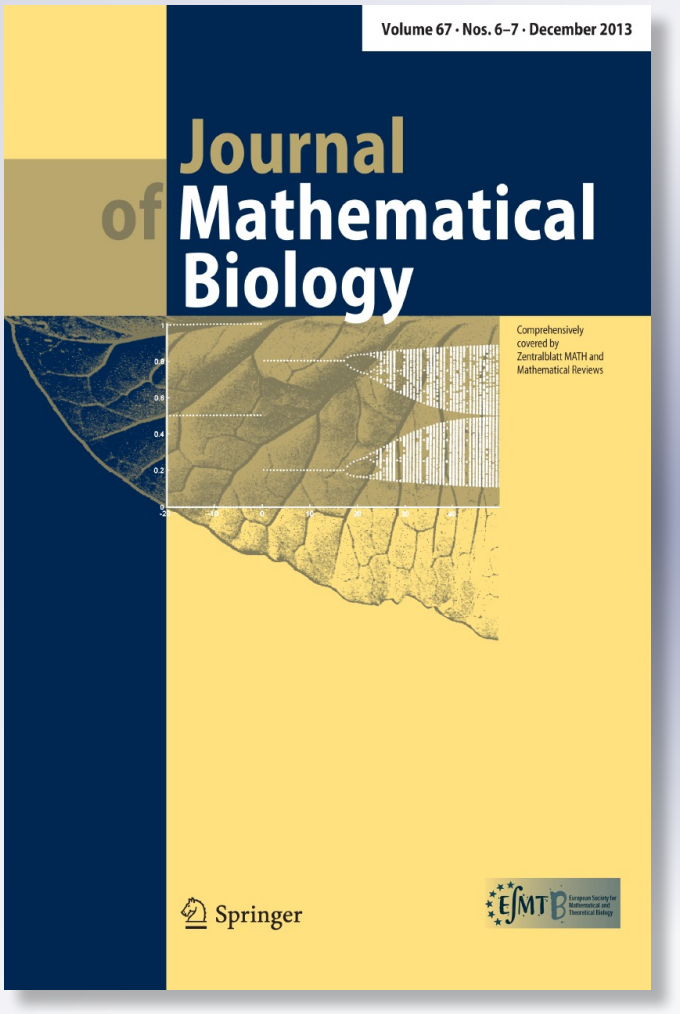

Springer

J. Math. Biol. (2013) 67:1847–1875
DOI 10.1007/s00285-012-0627-5

Mathematical Biology

Development and application of a volume penalization immersed boundary method for the computation of blood flow and shear stresses in cerebral vessels and aneurysms

Julia Mikhal · Bernard J. Geurts

Received: 18 March 2012 / Published online: 29 November 2012

Abstract A volume-penalizing immersed boundary method is presented for the simulation of laminar incompressible flow inside geometrically complex blood vessels in the human brain. We concentrate on cerebral aneurysms and compute flow in curved brain vessels with and without spherical aneurysm cavities attached. We approximate blood as an incompressible Newtonian fluid and simulate the flow with the use of a skew-symmetric finite-volume discretization and explicit time-stepping. A key element of the immersed boundary method is the so-called masking function. This is a binary function with which we identify at any location in the domain whether it is 'solid' or 'fluid', allowing to represent objects immersed in a Cartesian grid. We compare three definitions of the masking function for geometries that are non-aligned with the grid. In each case a 'staircase' representation is used in which a grid cell is either 'solid' or 'fluid'. Reliable findings are obtained with our immersed boundary method, even at fairly coarse meshes with about 16 grid cells across a velocity profile. The validation of the immersed boundary method is provided on the basis of classical Poiseuille flow in a cylindrical pipe. We obtain first order convergence for the velocity and the shear stress, reflecting the fact that in our approach the solid-fluid interface is localized with an accuracy on the order of a grid cell. Simulations for curved vessels and aneurysms are done for different flow regimes, characterized by different values of the Reynolds number (Re). The validation is performed for laminar flow at $Re = 250$,

J. Mikhal (✉) · B. J. Geurts
Multiscale Modeling and Simulation, Department of Applied Mathematics,
University of Twente, P.O. Box 217, 7500 AE Enschede, The Netherlands
e-mail: julia.mikhal@gmail.com

B. J. Geurts
Anisotropic Turbulence, Department of Applied Physics,
Eindhoven University of Technology, P.O. Box 513,
5600 MB Eindhoven, The Netherlands

while the flow in more complex geometries is studied at $Re = 100$ and $Re = 250$, as suggested by physiological conditions pertaining to flow of blood in the circle of Willis.

Keywords Immersed boundary method · Cerebral aneurysm · Incompressible flow · Shear stress

Mathematics Subject Classification (2000) 76D05 · 76M12 · 65M12

1 Introduction

There is a growing medical need to understand and predict the behavior of blood flow inside the human brain (Ku 1997; Wiebers et al. 1998). Healthy blood circulation depends on many factors among which are the properties of blood itself and the condition of the vessels through which blood flows. The walls of the blood vessels may become hard or weak over time, injured or infected and this can lead to different diseases such as atherosclerosis, the formation of aneurysms, thrombosis, stroke and others. Forces on vessel walls play a role in the progress of the disease, especially in the injured vessels (Castro et al. 2009). The prediction of the flow and stresses in the course of a gradually developing disease constitutes a challenging multiscale problem. This ranges from an analysis of short-time pulsatile flow to long-term medical prognosis. We are interested particularly in flow inside small cerebral vessels and aneurysms which may gradually develop due to weakening of the vessel walls. In this paper we show the use of an immersed boundary method to simulate incompressible Newtonian flow in complex vessels and aneurysm models. Numerically reliable results are obtained for a range of physiologically relevant conditions.

Understanding flow patterns inside an aneurysm may help to describe long-term effects such as the likelihood of the growth (Boussel et al. 2008) or even rupture (Shojima et al. 2004) of the aneurysm, or the accelerated deterioration of the vessel wall due to low shear stress (Doenitz et al. 2010). Such capability would allow a more complete planning of surgery and predict the effectiveness of certain procedures, and compare different options. Treatment of cerebral aneurysms often involves insertion of a slender coil. This procedure represents considerable risk and uncertainty about the long-term stability of coiled aneurysms (Sprengers et al. 2008; van Rooij et al. 2007). Numerical simulation could support decisions regarding, whether, which and how much coil to insert. It could also help in a follow-up monitoring of a patient.

A significant amount of work has been done on computational fluid dynamics (CFD) of flow in the human brain and in the cardiovascular system (Bernsdorf and Wang 2009; Cebral et al. 2005a; Gijsen et al. 1999; Janela et al. 2010; Ku 1997; Perktold et al. 1989; Quarteroni and Formaggia 2004). As a numerical approach, the finite element method is most commonly used to represent geometries of blood vessels. Often, the data are obtained from rather coarse biomedical imagery. The highly complex geometry is defined with some uncertainty by this imagery, and some smoothing and interface approximation need to be included to allow simulation with a body-fitted approach (Bernsdorf and Wang 2009; Cebral et al. 2005b; Gambaruto et al. 2011). As

an alternative approach the immersed boundary (IB) method was designed primarily for capturing viscous flow in domains of realistic complexity (Peskin 2002). In particular, we consider a volume penalization method. In this method, fluid is penalized from entering a solid part of a domain of interest by adding a suitable forcing term to the equations governing the fluid flow (Khadra et al. 2000). This method is also known as 'fictitious domain' method (Angot et al. 1999) and physically resembles the Darcy penalty method (Sarthou et al. 2007) or the Navier–Stokes/Brinkmann equations for flow in porous domains (Vasilyev and Kevlahan 2002). Here, we consider in particular the limit in which the porous domain becomes impenetrable and flow in complex solid domains can be represented. This method is discussed as one of the 'immersed boundary' methods in the recent review paper by Mittal and Iaccarino (2005), and in the sequel will be referred to as 'volume penalization immersed boundary method', a label that was also adopted in (Keetels et al. 2007).

Originally, the main motivation and application for IB methods was in simulation of the human heart by Peskin (a complete review is in (Peskin 2002)). Further, the IB method was widely applied in the bio-medical area. Among such applications are the modeling of sbiofilm processes (Dillon et al. 1996), arteriolar flow (Arthurs et al. 1998), swimming organisms (Cortez et al. 2004) and cell growth (Li et al. 2011). Another main sector of application of the IB method is in engineering, where classical problems are flow around a cylinder and around a road vehicle, flow in a wavy channel or inside a stirred tank (Iaccarino and Verzicco 2003), aerodynamics and parachute simulation by Kim and Peskin (2006), acoustic waves by Seo and Mittal (2011), and many others.

We present the development and application of an IB method for computing flow and shear stresses in cerebral aneurysms. As a numerical method we use the finite-volume discretization with a skew-symmetric treatment of the nonlinear convective fluxes. Flow is simulated at various flow conditions in several vessel geometries with and without aneurysm attached and shown to yield reliable results already at modest resolution. We concentrate on a generic model aneurysm with which the flow and forces are studied at a range of physiologically relevant Reynolds numbers.

The shape of cerebral aneurysms developing in patients can be inferred by using three-dimensional rotational angiography (Moret et al. 1998). In this procedure a small volume of brain tissue can be scanned, and aneurysms even of a size less than 3 mm can be depicted (van Rooij et al. 2008). This technique allows a reconstruction of three-dimensional arteries and aneurysms and hence an approximate identification of the fluid and the solid parts in the scanned volume. A volume-penalization IB method is applied to represent the aneurysm geometry. In the IB approach the domain is characterized by a so-called masking function, which takes the value '0' in the fluid part and '1' in solid parts of the domain. The raw angiography data allows for a simple 'staircase approximation' of the solid-fluid interface that defines the vessel and aneurysm shape. Individual voxels in the digital data form the smallest unit of localization of the solid-fluid interface. This raw information specifies the masking function in the sense that a computational cell is assigned to be 'solid' or 'fluid' on the basis of the digital imagery. We will adopt the 'staircase' geometry representation in this paper and do not incorporate any additional smoothing of the geometry or sophisticated reconstruction methods.

For a more complete modeling of the dynamics in the vessel system, flow-structure interaction often plays a role (Quarteroni and Formaggia 2004). In that case also parameters and models that characterize, e.g., mechanical properties of arterial tissue, influence of brain tissue and the influence of the cerebrospinal fluid are required. The amplitude of the wall motion in intracranial aneurysms was found to be less than 10 % of an artery diameter. Despite the rather modest motion of the vessel, over long time effects may accumulate. Even modest movement can affect the vessel walls, which might play a role in possible aneurysm rupture as was hypothesized in (Oubel et al. 2007). For realistic pulsatile flows some movement of the aneurysm walls was observed during a cardiac cycle (Oubel et al. 2010). In this paper we take a first step and restrict to developing the IB approach for rigid geometries. This allows to obtain the main flow characteristics inside relatively large cerebral aneurysms for which the relative wall movement can be neglected (Ku 1997).

The type of blood flow and the resulting forces on vessel walls depend largely on the shape of the vessel and on the viscosity of blood. These elements vary from one person to another, which makes the precise blood flow per heart beat a patient-specific characteristic that is hard to obtain. Rather, the patient's main flow structures that characterize the general type of blood motion and associated forces appear accessible by simulation and modeling. These are computational predictions, leading to patient-specific results of clinical value as suggested by (Cebral et al. 2005a,b; Hendrikse et al. 2005; Kamath 1981). The distribution of shear stresses at the vessel wall and the flow pattern inside the aneurysm are considered to be relevant to characterizing the general quality of circulation. Regions of high and low shear stress are often visualized as potential markers for aneurysm growth. High shear stress levels were reported near the 'neck' of a saccular aneurysm, and may be relevant during the initiating phase (Shojima et al. 2004). Low Wall Shear Stress has been reported to have a negative effect on endothelial cells and may be important to local remodeling of an arterial wall and to aneurysm growth and rupture (Boussel et al. 2008). A low wall shear stress may facilitate the growing phase and may trigger the rupture of a cerebral aneurysm by causing degenerative changes in the aneurysm wall. The situation is, however, more complex, as illustrated by the phenomenon of spontaneous stabilization of aneurysms after an initial phase of growth (Koffijberg et al. 2008). It is still very much an open issue what the precise correlation is between shear stress patterns and general circulation on the one hand, and developing medical risks such as aneurysm rupture, on the other hand. In this complex problem, haemodynamic stimuli are but one of many factors.

Cerebral aneurysms are most often located in the circle of Willis—the central vessel network for the supply of blood to the human brain. Common risk-areas are at 'T' and 'Y'-shaped junctions in the vessels (Hendrikse et al. 2005). This motivates to analyze the flow in basic vessels and aneurysms by modeling them as curved cylindrical tubes to which spherical cavities are attached. This choice is not restrictive for the development of the computational approach; rather it constitutes a stepping stone problem toward simulation of actual patient-based geometries. The computational model for the simulation of blood flow through the larger vessels in the human brain is based on the incompressible Navier–Stokes equations. In this paper we illustrate the IB approach by predicting flow in basic curved cylindrical and spherical geometries.

A primary challenge for any CFD method, whether it is a body-fitted method (Hirsch 1988) or an IB method (Peskin 2002; Mittal and Iaccarino 2005; Iaccarino and Verzicco 2003), is to capture the flow near solid-fluid interfaces. In this region the highest velocity gradients may occur, leading to correspondingly highest levels of shear stress, but also potentially highest levels of numerical error. In methods employing body-fitted grids, the quality of predictions is directly linked to the degree to which grid-lines can be nearly orthogonal to the solid-fluid interface and to each other. Also, variation in local grid sizes is a factor determining numerical error. Since the generation of a suitable grid is often very challenging, the raw data defining the actual aneurysm geometry often require considerable smoothing, segmentation and geometric operations eliminating small side vessels that are felt not to be too important for the flow. On the positive side, the main benefit of a body-fitted approach is that discrete variables are situated also at the solid-fluid interface, which makes implementation of no-slip boundary conditions quite straightforward. Hence, in body-fitted approaches the no-slip property can be accurately imposed, but only on a 'pre-processed' smoothed and often somewhat altered geometry (Gambaruto et al. 2011; Cebral et al. 2005b).

Capturing flow near complex shaped solid-fluid interfaces is equally challenging in an IB method. In our IB approach, the actual geometry of the aneurysm can be extracted directly from the voxel information in the raw medical imagery, without the need for smoothing of the geometry. Grid generation is no issue for IB methods since the geometry of the flow domain is directly immersed in a Cartesian grid. The location of the solid-fluid interface is known only up to the size of a grid cell, and the shape of the interface is approximated using a 'staircase' representation, stemming from the fact that any grid cell is labeled either entirely 'solid' or entirely 'fluid'. Refinements in which a fraction between 0 and 1 of a cell can be fluid-filled (Cheny and Botella 2010) are not taken into consideration here. In fact, the medical imagery from which we start has a high, but still quite limiting spatial resolution arranged in voxels. This calls more for a systematic assessment of the sensitivity of predictions to uncertainties in the flow domain (Mikhal and Geurts 2011) than for adaptations of the domain by smoothing and interface reconstruction as would be considered in higher-order methods (Gao et al. 2007). Without relaxing the staircase approximation, the problem of capturing near-interface properties can only be addressed by increasing the spatial resolution. In this paper we study for curved vessels and model aneurysms the error-reduction upon increasing the spatial resolution. We establish first order convergence of both the velocity field and its spatial derivatives for Poiseuille flow. Convergence is also assessed more qualitatively by systematic grid-refinement for flow in complex geometries.

Numerical accuracy was investigated extensively for a second-order IB method in (Lai and Peskin 2000; Griffith and Peskin 2005). Simulation results for sufficiently smooth solutions were analyzed and actual second order convergence for the velocity and pressure fields was observed. No results were included for convergence of the gradient of the velocity. For a volume penalizing IB method applied to Stokes flow, i.e., very viscous, smooth flow, it was shown rigorously in (Mori 2008) that first-order convergence of the velocity field can be expected, which was actually achieved in test simulations. In case the solid-fluid interface is allowed to be smoothed, or if it is already sufficiently smooth by itself, a so-called ghost-cell IB method can be shown to yield first order (Berthelsen and Faltinsen 2008) or in selected situations second order

(Gao et al. 2007) converging velocity fields for flow over an undulating channel (Tseng and Ferziger 2003). In this reference, a direct comparison between a body-fitted and an IB method was also made for the shear stress at a selected flow condition - the results were found to be nearly identical. A comparable result may be found in (Kang et al. 2009) where a study is made of the accuracy with which turbulent wall pressure fluctuations can be predicted for sufficiently smooth surfaces. In this paper we extend the convergence study and show first-order convergence of velocity and shear stress in complex domains also in combination with the staircase approximation of the interfaces.

The quality of predictions depends strongly on the spatial resolution that can be adopted. From a study of Poiseuille flow we will show that about 16 grid points across a velocity profile suffice to obtain reliable flow predictions, e.g., yielding an L_2-norm of the error with respect to the exact solution less than 0.1. For general geometries that are not aligned with the underlying Cartesian grid, first order convergence upon grid-refinement is established. This convergence order is associated with the non-alignment of the geometry with the underlying Cartesian grid. Using an energy-conserving skew-symmetric discretization by Verstappen and Veldman (2003) the IB approach was found to provide the main flow structure and associated stress levels. Flow emerging from a steady pressure drop was investigated and the laminar velocity field and shear stress distribution were computed. Flow in curved vessels and model aneurysms is considered at $Re = 100$ and $Re = 250$ to comply with clinical data in (Kamath 1981; Quarteroni and Formaggia 2004). At the higher Reynolds number the flow displays some unsteadiness, consistent with findings of Gambaruto et al. (2011), associated with the nonlinearity in the Navier–Stokes equations, even at constant flow rate.

The organization of this paper is as follows. In Sect. 2 we present the computational model, based on the IB method and we discuss the strategies to generate the masking function. We validate the IB method for Poiseuille flow in Sect. 3 and discuss the convergence of numerical predictions. An analysis of shear stress levels in model vessels and aneurysms is given in Sect. 4. Concluding remarks are in Sect. 5.

2 Computational model for flow inside cerebral aneurysms

In this section we first present the incompressible Navier–Stokes equations as the mathematical model describing the flow of blood inside the human brain (Sect. 2.1). Then we describe the numerical method to perform simulations of the flow (Sect. 2.2). A key element of the adopted IB method is the 'masking function', which identifies for each point in space whether it is 'solid material' or 'fluid domain'. In Sect. 2.3 we look into how masking functions are generated and introduce the model geometries.

2.1 Incompressible flow in complex domains

There are various approaches to model flow of blood in the human brain. A comprehensive overview is given by Quarteroni and Formaggia (2004). In one approach, the blood is approximated as a Newtonian fluid (Cebral et al. 2005a). More refined models, e.g., the Carreau–Yasuda model, include the shear-thinning behavior of blood and

allow to capture non-Newtonian rheology (Bernsdorf and Wang 2009; Gijsen et al. 1999; Janela et al. 2010). Under physiological flow conditions in sufficiently large arteries the non-Newtonian corrections were found to be quite small (Cebral et al. 2005b; Gijsen et al. 1999; Janela et al. 2010; Perktold et al. 1989). The main flow characteristics appeared to be the same as for a Newtonian fluid at somewhat different stress and velocity levels.

In this paper we concentrate on arteries of the circle of Willis. Typical fine-scale structures in the blood are on the order of 10^{-6} m. A length-scale that characterizes the cross section of a typical cerebral vessel inside the circle of Willis is on the order of 10^{-3} m (Kamath 1981). This difference in length-scale of three orders of magnitude motivates to approximate blood as an incompressible Newtonian fluid (Quarteroni and Formaggia 2004).

A common location of cerebral aneurysms within the circle of Willis is on the internal carotid artery (ICA), where a typical volumetric flow-rate is reported to be $Q_r^* = 245 \pm 65$ ml/min (Hendrikse et al. 2005), while the diameter of the ICA is approximately $D^* = 0.42 \pm 0.09$ cm (Kamath 1981), leading to a reference velocity $U_r^* = 0.2947$ m/s and a corresponding Reynolds number estimated as $Re = 177$ computed by $Re = U_r^* L_r^* / \nu_r^*$ in which we used as reference length the radius of the artery $L_r^* = R^* = D^*/2$ and a kinematic viscosity $\nu_r^* = 3.5 \cdot 10^{-6}$ m^2/s (Quarteroni and Formaggia 2004). The Reynolds number Re is the only parameter which is required to specify the flow conditions. It quantifies the ratio between the magnitude of the (destabilizing) convective transport and the (stabilizing) viscous processes. It is well known that for relatively low Reynolds numbers flow is laminar and steady (Young et al. 1997), which implies a smooth velocity and pressure field. With increasing Reynolds number the flow can develop more detailed vortical structures, e.g., associated with separated flow near abrupt changes in the shape of a vessel. A further increase in Re usually implies that the flow becomes unsteady and the range of vortices becomes much wider (Young et al. 1997). The range of Reynolds numbers arising in the flow in the circle of Willis, as estimated above, corresponds to laminar, possibly unsteady flow.

The Navier–Stokes equations provide a full representation of Newtonian fluid mechanics, expressing conservation of mass and momentum. The total physical domain Ω, consists of a fluid part Ω_f and a solid part Ω_s. The interface between the two will be identified as $\partial\Omega$ at which no-slip conditions apply. The governing equations are given in dimensional form by:

$$\frac{\partial \mathbf{u}^*}{\partial t^*} + \mathbf{u}^* \cdot \nabla^* \mathbf{u}^* = -\nabla^* \left(\frac{p^*}{\rho^*}\right) + \nu^* \nabla^{*\,2} \mathbf{u}^* + \frac{\mathbf{f}^*}{\rho^*} \tag{1}$$

$$\nabla^* \cdot \mathbf{u}^* = 0 \tag{2}$$

Here $\mathbf{u}^*$ is the velocity of the fluid, ρ^* is mass density, p^* the pressure and $\mathbf{f}^*$ a forcing term that will play a central role in this paper as it is used to represent the impenetrability of complex shaped solid vessel walls, i.e., the no-slip condition. By choosing reference velocity U_r^* and reference length L_r^* we can express in a standard way reference time as $t_r^* = L_r^*/U_r^*$. Using reference density $\rho_r^* = \rho^*$ we find a reference pressure as $p_r^* = (U_r^*)^2 \rho_r^*$. For the forcing term we select a direct volume penalization in which

$$\frac{\mathbf{f}^*}{\rho^*} = -\frac{1}{\varepsilon^*} H\mathbf{u}^* \tag{3}$$

where ε^* is a forcing time scale and H is the masking function: $H(\mathbf{x}) = 1$ if $\mathbf{x} \in \Omega_s$ and $H(\mathbf{x}) = 0$ if $\mathbf{x} \in \Omega_f$. Based on the reference velocity and length we set the reference forcing time scale as $\varepsilon_r^* = L_r^*/U_r^* = t_r^*$, which suggests that by wishing $\varepsilon \ll 1$ the dimensional control parameter $\varepsilon^* = \varepsilon_r^* \varepsilon \ll \varepsilon_r^* = t_r^*$, i.e., much smaller than the reference time scale.

After choosing all reference parameters we obtain the non-dimensional form of the Navier–Stokes equations:

$$\frac{\partial \mathbf{u}}{\partial t} + \mathbf{u} \cdot \nabla \mathbf{u} = -\nabla p + \frac{1}{Re} \nabla^2 \mathbf{u} - \frac{1}{\varepsilon} H\mathbf{u} \tag{4}$$

$$\nabla \cdot \mathbf{u} = 0 \tag{5}$$

In this paper we will consider only stationary, i.e., non moving walls. By adding the forcing to the incompressible momentum equations we formally arrive at the Brinkman equation for flow in a porous medium with permeability related to the parameter ε (Liu and Vasilyev 2007). Note that, with the inclusion of $\mathbf{f}$ as in (3) we arrive at a one-velocity field model for the flow in the entire domain Ω.

The basis of the volume penalization method is the masking function which distinguishes fluid parts from solid parts of the domain. In regions where $H = 0$ the Navier–Stokes system is solved. In the solid regions $H = 1$ and the forcing is dominant if the non-dimensional parameter ε is very small. As a result, the governing equation reduces to $\partial_t \mathbf{u} \approx -\mathbf{u}/\varepsilon$ if $|\mathbf{u}| \gg \varepsilon$ in the solid domain. Hence, any nonzero $\mathbf{u}$ is exponentially sent back to $\mathbf{0}$ on a time-scale ε. If $|\mathbf{u}| \leq \varepsilon$ the forcing is not dominant in the solid, but control over $|\mathbf{u}|$ is already obtained, i.e., $|\mathbf{u}|$ takes on negligible values in the solid. We take $\varepsilon = 10^{-10}$ relative to the dimensionless time-scale L_r/U_r in the sequel. Such low values of the control parameter ε imply that the forcing term effectively yields a Brinkman equation in which 'porous' regions are virtually impenetrable, i.e., solid material. The detailed specification and the ways of generating the masking function are presented later in Sect. 2.3.

2.2 Numerical method for simulating incompressible flow with an immersed boundary approach

In this subsection we sketch the numerical method used for the simulation of flow through complex shaped domains. First, we describe the direct numerical simulation approach and specify the volume penalization IB method afterwards.

We employ a staggered allocation of the flow variables $(\mathbf{u}, p) = (u, v, w, p)$ as basis for our flow solver (Geurts 2003). In two dimensions this is sketched in Fig. 1, where a primary grid cell with the pressure defined in the center and the Cartesian velocity components at the cell surfaces is presented. The locations at which the velocities and the pressure are stored are referred to as the velocity- and the pressure-points, respectively. In addition, we introduce the corner-points of the primary grid cells as relevant locations for the definition of the IB method later on.

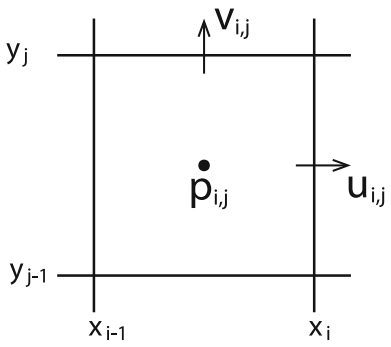

Fig. 1 Sketch of a primary grid cell in 2d with staggered allocation of the variables. The pressure p is in the middle of the grid cell, while the velocities (u and v) are defined at the centers of the faces

The principles of conservation of mass and momentum as expressed in (4) and (5), form the basis for the discrete computational model that is used for the actual simulations. In the Navier–Stokes equations (4) the rate of change of momentum is obtained from the nonlinear convective flux, the linear viscous flux, the gradient of the pressure and the contribution from the forcing term. These contributions to the total flux each have a particular physical character that needs to be represented properly in the discrete formulation. In particular, the convective flux is skew-symmetric, implying that this flux only contributes to the transport of kinetic energy of the solution in physical space; it does not generate nor dissipate this energy. An important contribution to second-order skew-symmetric discretization of the convective terms in the Navier–Stokes equations is in the work of Morinishi et al. (1998), which motivated later work of Verstappen and Veldman (2003) upon which we rely here. These are examples of a more general philosophy of developing discretization schemes which 'respect' basic properties of the underlying system of equations, knows as mimetic discretization (Shashkov and Steinberg 1995). Likewise, the viscous flux contributes only to dissipation of energy, which has to be strictly maintained in a numerical method.

In this paper we employ symmetry preserving finite volume discretization and use central differencing of second order accuracy, which maintains explicitly the skew-symmetry in the discrete equations. Since the energy is preserved under the convective operator the skew symmetric discretization allows to obtain a stable solution on any grid. For proper capturing of the solenoidal property (5) of the velocity field we approximate the gradient operator by the transpose of the numerical divergence operator and a positive definite discretization of the viscous terms, closely following Verstappen and Veldman (2003). The contributions of the convective, viscous and pressure-gradient fluxes are integrated in time using a generalization of the explicit second order accurate Adams-Bashforth method. Care is taken of accurately representing the skew-symmetry also in the time-integration. Full incorporation would require an implicit time-stepping, which, however, is computationally too demanding. Instead, time-integration starts from a modification of the leapfrog method with linear inter/extrapolations of the required 'off-step' velocities and an implicit treatment of the incompressibility constraint. Optimization for largest stability region of the resulting scheme yields a particular so-called 'one-leg' time-integration method,

with a mathematical structure that is akin to the well-known Adams-Bashforth scheme. More details can be found in (Verstappen and Veldman 2003).

A special role is played by the forcing term in the Navier–Stokes equations (4), which represents the volume penalization accounting for solid objects inside and at the boundaries of the flow domain. The role of the forcing term is to yield an accurate approximation of the no-slip condition at solid boundaries. In conventional computational fluid dynamics such a forcing term is not needed since the flow domain is endowed with a body-fitted grid on which the equations are discretized. The grid-lines in such cases are defined such that they either closely follow the contours of the solid boundaries, or they are (preferably) at right angles with them. In such a discrete formulation the no-slip boundary condition can be imposed easily. The body-fitted grid is efficient if the fluid domain Ω_f is not too complex and does not contain too many separate objects around which the fluid should flow (Kovalev 2005). For considerably more complex flow domains or in case the location of the solid-fluid interface is not perfectly known, as in case of medical imagery, the body-fitted grid approach is limited by the generation of suitable meshes. These should not only align with the solid boundaries, but also be sufficiently smooth near these boundaries to allow an accurate solution in the boundary layers (Löhner 2007). In our discrete model the forcing term contributes strongly to the stiffness of the equations. When an explicit time-stepping method would be adopted for the forcing term, as is done for the other dynamic contributions, this would result in extremely small time-steps in view of numerical stability. Therefore, the linear forcing term is integrated in time using the implicit Euler scheme (Lopez Penha et al. 2011).

2.3 Masking function strategy

In this subsection, we first consider three options for creating a general masking function and illustrate these for a circle on a 2d Cartesian grid. We also present the procedure with which the specification of the masking function of any curved cylindrical 3d-tube was taken up. The validation and comparison of the masking strategies will be presented in Sect. 3.

The masking function technique is a simple and fast way to indicate the location of an object. Illustration of the masking function for a flow domain is given in Fig. 2. A simple approach to distinguish which grid cells are inside the solid domain and which are outside is the following: if the center of the grid cell is of type 'solid' or 'fluid', then that entire grid cell is taken to be of that type. Fig. 2(b) illustrates how, based on this rule, some cells become internal (hatched) and others are outside the fluid part of the domain.

In three-dimensional domains we formulate the problem in a rectangular block of size $L_x \times L_y \times L_z$ that is large enough to contain the flow domain of interest. A uniform Cartesian grid with mesh-spacings $h_{x,y,z} = L_{x,y,z}/N_{x,y,z}$ for the three coordinate directions is defined, using $N_{x,y,z}$ grid cells in each direction. In our basic method, if the center of a cell is solid (fluid) then we take the whole cell to be solid (fluid) and $H = 1$ ($H = 0$) (Fig. 3a). Next to this basic method we can introduce two closely related methods based on the corner-nodes of a grid cell. We consider 3d cells and first determine the solid or fluid property for every corner point of the cell. Then,

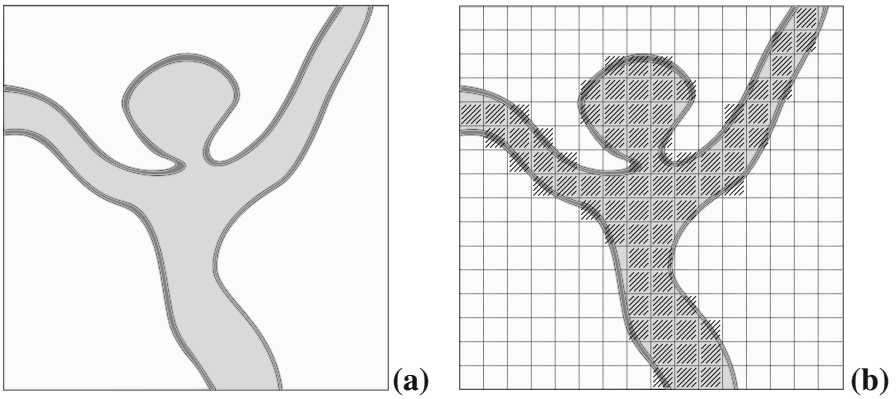

Fig. 2 Sketch of complex flow domain (**a**) (*grey area*). On a Cartesian grid the definition of the masking function can be based, e.g., on the 'material' ('solid' or 'fluid') found at the cell center (**b**)

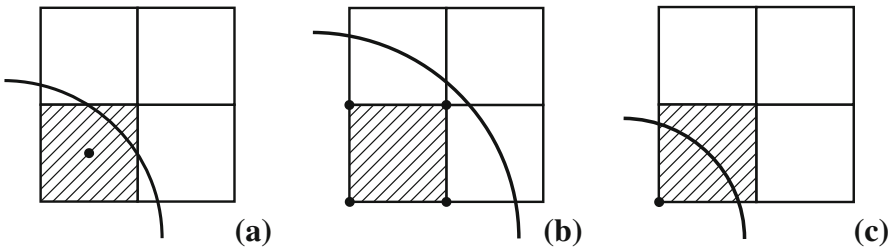

Fig. 3 Strategies to define a masking function for a grid cell on a Cartesian grid. For convenience we illustrate here 2d grid cells. We propose three ways to define fluid cells (hatched) and thus the fluid domain. The 'basic' strategy (**a**) is the one where the property at the center of the cell defines that of the whole cell. The two other strategies differ in the number of corner points that are inside the fluid domain. Thus we obtain the so-called 'inner' strategy (**b**) when the cell is denoted to be 'fluid' if all its corners are inside the fluid domain and the 'outer' strategy (**c**) when we call the cell 'fluid' if at least one of its corners belongs to the fluid domain

in one strategy we denote a grid cell as fluid if all eight of its nodes are fluid. This is illustrated for 2d-cells in Fig. 3b (fluid cell is hatched). Another strategy assigns for the whole cell the value 'fluid' if at least one of its corners is in the fluid part of the domain (Fig. 3c). In the sequel, we will refer to these three strategies as 'basic', 'inner' and 'outer' respectively. The 'inner' strategy has the tendency to produce flow domains that are slightly smaller than the 'basic' approach while the 'outer' strategy is likely to yield slightly larger flow domains. In the next section we will validate these three masking function strategies for Poiseuille flow in a straight cylindrical pipe, showing the sensitivity of predictions to details of the geometry definition. The possible application of the 'inner' and 'outer' masking strategies was presented in (Mikhal and Geurts 2011), where 'inner' and 'outer' solutions were considered as numerically bounding the 'basic' solution and some of its important flow characteristics.

The masking strategies define the masking function in the middle of the grid cell, i.e., in H_p points of a staggered grid. Given H_p, we can extract H_u, H_v and H_w for the staggered grid. We assign the value of the masking function at a cell face as the maximum

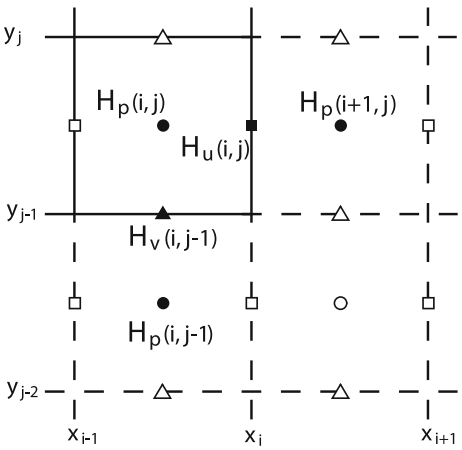

Fig. 4 The process of defining masking function in the staggered locations (*squares*, *triangles*), based on the values in the middle of the cell (*circles*). We choose the maximum value of two H_p values of neighboring cells sharing a common face and assign this value to the staggered masking function H_u or H_v. This reflects the choice that if a solid and a fluid cell come together in a face then the face is solid as well

of the H_p values of the neighboring grid cells. In Fig. 4 we illustrate for 2d grid cells the mechanism of extracting staggered masking values at the grid faces. Thus, $H_u(i, j) = \max(H_p(i, j), H_p(i + 1, j))$ and $H_v(i, j - 1) = \max(H_p(i, j), H_p(i, j - 1))$.

To obtain a masking function according to one of the above strategies for a smoothly curved cylindrical tube we use the smallest distance approach to specify for every point in the computational domain its 'type', i.e., solid or fluid. In fact, we determine the minimum distance to the centerline of the curved vessel and then check the condition whether this distance is smaller or greater than the radius of the desired cylindrical tube. We apply the smallest distance approach to the centers of the cells in the 'basic' strategy and to all eight nodes of the 3d-cell in the 'inner' and 'outer' strategies.

We consider the centerline of the tube in parametric form, as $(x(s), y(s), z(s))$ where $0 \leq s \leq 1$. For every point (X, Y, Z) in the computational domain we may determine whether or not the minimal distance to the centerline is smaller than the radius of the desired cylindrical tube. If so, then the point is in the fluid domain, otherwise it is in the solid domain. Specifically, we consider the distance vector

$$\mathbf{d} = \Big(X - x(s), Y - y(s), Z - z(s)\Big) \tag{6}$$

and obtain the square of the Euclidean distance as the inner product

$$D \equiv \mathbf{d} \cdot \mathbf{d} = |\mathbf{d}|^2 \tag{7}$$

For every (X, Y, Z), D is a function of the parameter s only. We require the global minimum of the function D, which implies at least the first order condition

$$D' = 2\mathbf{d} \cdot \mathbf{d}' = 0 \tag{8}$$

where the prime indicates differentiation with respect to s. This optimality condition specifies that in the optima the distance vector $\mathbf{d}$ is perpendicular to the tangential vector $\mathbf{d}'$ at the centerline, which has an obvious geometric interpretation. The equation

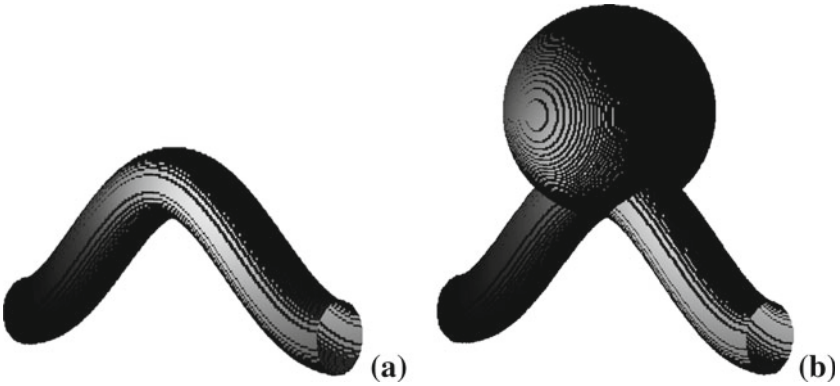

Fig. 5 Basic geometries in 3d. The curved vessel (**a**) is a cylindrical tube with a sinusoidal centerline, while the model aneurysm is composed of a curved vessel and a sphere attached to it (**b**)

for an extremum is

$$\Big(X - x(s)\Big)x'(s) + \Big(Y - y(s)\Big)y'(s) + \Big(Z - z(s)\Big)z'(s) = 0 \tag{9}$$

which can be solved numerically to obtain local (and global) extrema for $0 \leq s \leq 1$. In the sequel we consider planar curves as centerline. In that case $y' = 0$ and $x(s) = L_x s$ so that

$$-L_x^2 s + \Big(Z - z(s)\Big)z'(s) = -XL_x \tag{10}$$

As a particular case we take $y(s) = L_y/2$ and choose the centerline to be sinusoidal

$$z(s) = L_z/2 + C\sin(2\pi(s - 1/4)) \tag{11}$$

where C is called the 'curve-parameter', for simplicity.

In order to specify the 'type', i.e., solid or fluid, of a given point (X, Y, Z) we need first to determine the parameter-value s at which the global minimum of (9) is attained. Numerically, this can be implemented in two stages: first, we coarsely sample the square distance function (7) in 2^k steps to obtain a 'candidate' interval and second, we refine this interval to obtain the global minimum using simple bisection. After some experimentation we found that coarse sampling at $k = 6$ is suitable for mildly curved vessels. Once the optimal s^* is determined for a given (X, Y, Z), we can compute the smallest distance d at s^*. If this smallest distance $d \leq R$ then (X, Y, Z) is of type 'fluid', and it is of type 'solid' otherwise.

In this paper we consider two basic geometries motivated by medical application: curved vessels and model aneurysms. Three dimensional shapes are illustrated in Fig. 5. The curved vessel is a cylindrical tube, with a sinusoidal centerline (Fig. 5a) where the curve-parameter $C = 2$ in (11). The model aneurysm (Fig. 5b) is the 'extension' of this curved vessel by merging it with a sphere, with radius $R_{sphere} = 3R_{vessel}$ (Fig. 5b).

3 Validation of the IB method

In this section we analyze the capabilities of the IB method in capturing steady flow in non-aligned geometries and show the results of computations for a number of basic geometrical shapes such as a straight cylindrical vessel and smoothly curved cylindrical vessels. In the first subsection we focus on Poiseuille flow in a straight vessel and provide an assessment of the accuracy of the IB method. The total IB method is shown to have first order convergence. Subsequently, we propose a qualitative view of the flow inside curved vessels, showing the flexibility of the IB approach in predicting flow in more complex flow domains, and quantify the level of convergence by monitoring the pressure drop over the vessel at a range of resolutions.

3.1 Flow in straight vessels

A fully developed, incompressible, laminar flow through a straight circular tube of constant cross section is known as Poiseuille flow (Batchelor 2007). The exact analytical solution for this type of flow can be written as $(u, v, w) = (u, 0, 0)$, where $u(r) = 1 - r^2$ in terms of the radial coordinate r. This corresponds to a volumetric flow rate $Q = \frac{\pi}{2}$.

The IB method is validated by comparing the numerical results with the analytical solution for cylindrical pipe flow. We consider flow at $Re = 250$ and assume that the x-domain is from $-L/2$ to $L/2$ with center of the tube at $x = 0$, and likewise for the y and z-domain ranging from $-3R/2$ to $3R/2$ with center at $y = 0$ and $z = 0$. Since we adopt a non-dimensional formulation, the validation of the numerical method with reference to laminar Poiseuille flow can be executed at any value of Re as long as the parabolic velocity profile is stable. Identical results can be obtained when validation is done at lower Reynolds numbers. To test the application of the method at physiologically relevant conditions, we set $Re = 250$; at this flow condition a longer simulation time is required to reach the final steady state that we want to test against the analytical solution. This provides as additional result a test of the time-stepping method under realistic conditions.

Numerically, we define the flow to have reached the steady state once the pressure drop over the computational domain needed to maintain the desired flow rate has converged to within 10^{-8}. During the simulations we verified that the flow is independent of the axial coordinate, as required by the analytical solution.

We investigate numerical velocity profiles for a number of grid resolutions. We use $4 \times N \times N$ grid cells in the x, y and z directions respectively, where $N = 8, 16, \ldots, 256$. As was already mentioned in Sect. 2.3 we may create masking functions in three different ways. In order to investigate the accuracy and robustness of the IB method we validate each of these masking strategies. Figure 6 illustrates velocity profiles for all three masking strategies. The solid line denotes the analytical solution, all dashed lines are approaching this solution from above or below, depending on whether the numerical representation of the circular cross section is slightly smaller or slightly larger than the actual cross-section, respectively. Combination of the 'inner' and 'outer' masking strategies provides a practical manner to arrive at lower and

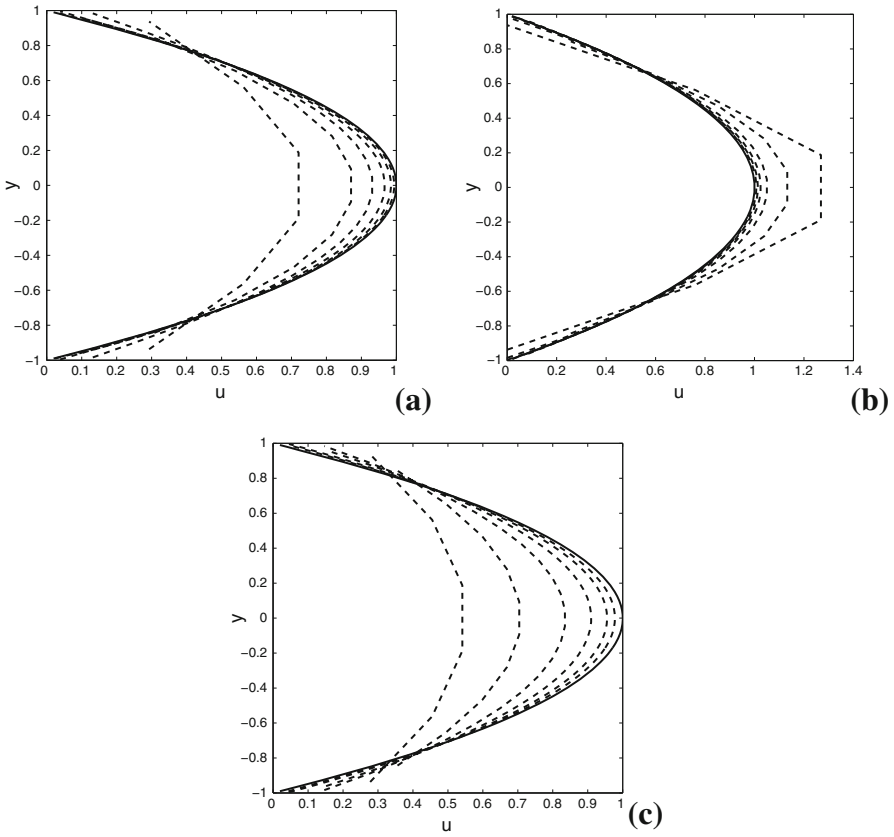

Fig. 6 Velocity profiles for three different masking function strategies ('basic'—(**a**), 'inner'—(**b**), 'outer'—(**c**)). The total flow domain ranges from $-3/2 \leq y \leq 3/2$, $-3/2 \leq z \leq 3/2$, of which the profile at $z = 0$ and $|y| \leq 1$ is shown. Profiles are obtained at grid resolutions $4 \times N \times N$ in (x, y, z) with $N = 8, 16, \ldots, 256$. Solutions at increasing resolutions are identified by the sequence of *dashed lines* which converge to the solid line representing the analytical solution for Poiseuille flow

upper bounding solutions between which the analytical solution is contained. This was exploited and presented in (Mikhal and Geurts 2011). The visual convergence check will next be quantified and the order of accuracy of the IB method inferred.

There are several ways to define the difference between analytical and numerical solutions. For estimating the convergence of the velocities we compare numerical results with the analytical solution directly in the grid points and compute the discrete L_2-norm along a line at $z = 0$ and $x = 0$, i.e., along a vertical line in the middle of the domain. The difference between the analytical and a numerical solution appears as

$$\delta_u = \sqrt{\frac{1}{N} \sum_j (u_{N_x/2, j, N_z/2} - U_{ex,j})^2}, \tag{12}$$

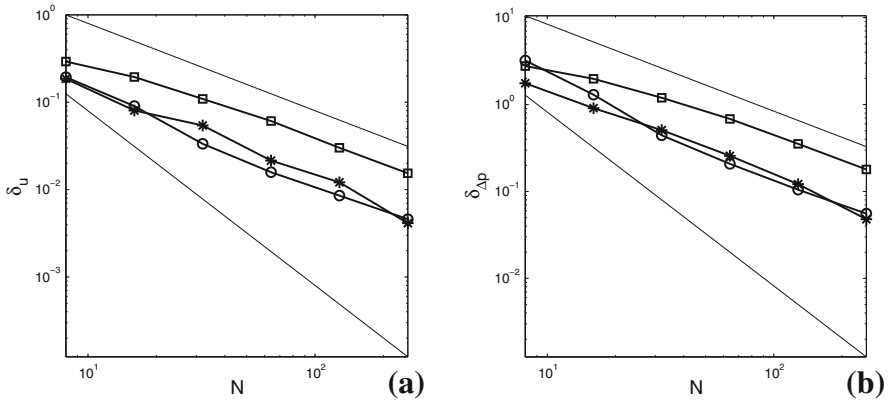

Fig. 7 Convergence of the numerical solution for velocities (**a**) and pressure differences (**b**) for Poiseuille flow. The difference for the velocities is measured in terms of the discrete L_2-norm δ_u, while for the pressure difference we consider the absolute difference between analytical and numerical solutions. *Solid lines* without markers denote slopes -1 and -2 respectively. The *line* marked with *circles* corresponds to the 'inner' strategy, the line with *asterisks* is for the 'basic' strategy, the line with *squares* is for the 'outer' strategy for generating the masking function

where $u_{N_x/2,j,N_z/2} = u(\frac{1}{2}N_x, j, \frac{1}{2}N_z)$ and $U_{ex,j} = (1 - y_j)^2$ for grid points $|y_j| \leq 1$. We also analyze the convergence of the pressure differences over the computational domain, by computing the absolute value of the difference between the numerical and analytical pressure differences. The reduction of the error for velocity and pressure difference is presented in Fig. 7 for all the strategies. Solid lines show slopes at -1 and -2 as reference. The marked lines are for the three masking strategies. As we can observe, for all masking strategies the numerical method converges to first order. This basically reflects the non-alignment of the cylinder wall with the Cartesian grid, leading to inaccuracies in the solid-fluid interface definition. It appears in this case that the 'inner' masking strategy is most accurately representing Poiseuille flow closely followed by the 'basic' strategy. For further computations we will use the 'basic' masking function based on the pressure-points (Fig. 3a), as this is most straightforward.

3.2 Flow in curved vessels

In the previous subsection we assessed the numerical method for a basic case of flow in a straight cylindrical tube. The validation shows first order convergence for laminar Poiseuille flow. However, the geometry of blood vessels in a human brain is much more complicated. The first step towards simulating flow in more realistic vessel shapes is to consider smoothly curved geometries. In this subsection we show the flexibility of the IB method to capture flow in curved vessels even at fairly modest resolutions. The steady velocity field that develops at $Re = 1$ is shown in Fig. 8 for curved vessels with curve-parameters $C = 1$, $C = 2$, $C = 5$ and $C = 10$ in (11). Simulations show that the laminar flow closely follows the shape of the vessel. Near the vessel wall we recognize the coarseness of the 'staircase' representation. This effect is seen to be only very local and can be reduced by increasing the resolution.

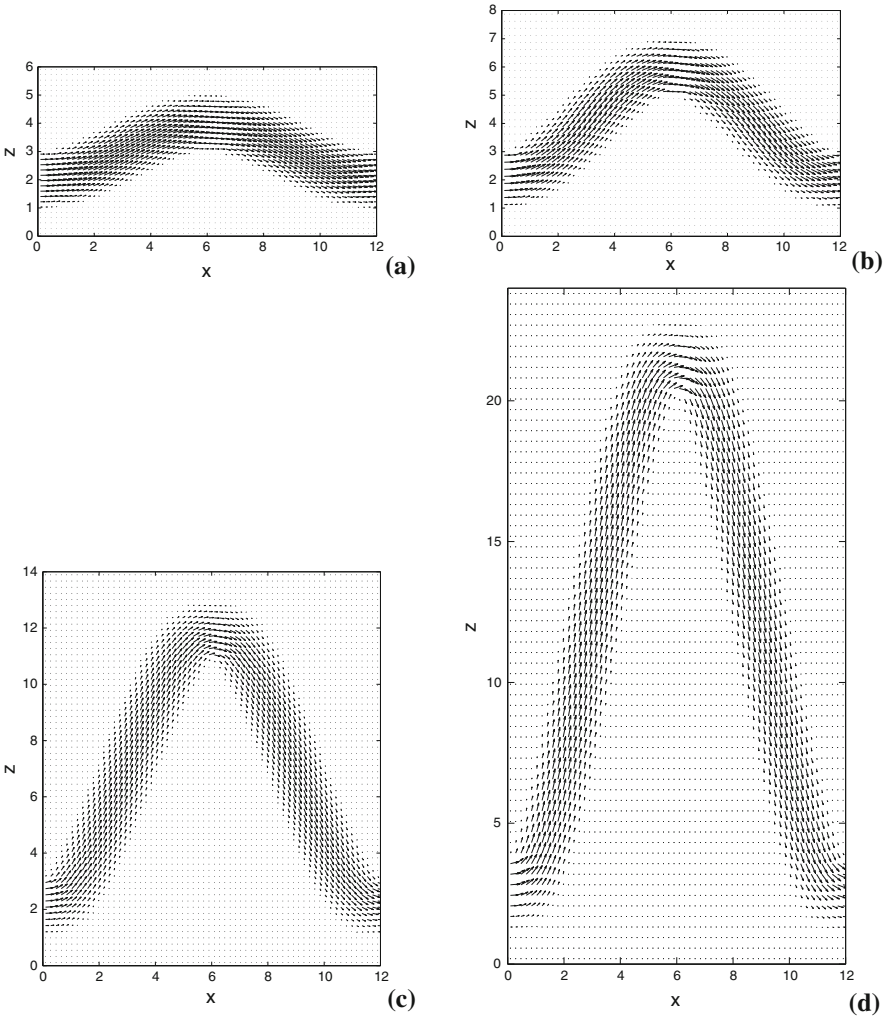

Fig. 8 Velocity vector fields at $Re = 1$ in middle cross-sections of sinusoidally curved cylindrical vessels at increasing values of the curve-parameter in (11): $C = 1$ (**a**), $C = 2$ (**b**), $C = 5$ (**c**) and $C = 10$ (**d**). Simulations employed a resolution of $64 \times 16 \times 32$ for (**a**), (**b**) and $64 \times 32 \times 64$ for (**c**), (**d**)

The velocity profiles along the curved tubes depend on the actual shape of the vessel. The profiles follow the contours of the vessel and at certain locations along the centerline the local profiles differ considerably from the simple Poiseuille profile that was considered earlier. This is shown in Fig. 9. Already at relatively coarse grids the numerical solution appears to capture the flow quite reliably.

The convergence of the IB method for curved vessels and model aneurysms can be further quantified. We consider the pressure difference over the flow domain in the x-direction that is required to maintain the imposed volumetric flow rate. In Fig. 10 we display the development of this pressure difference for two flow regimes, i.e., at $Re = 1$ (Fig. 10a) and $Re = 100$ (Fig. 10b) for a curved vessel at curve-parameter

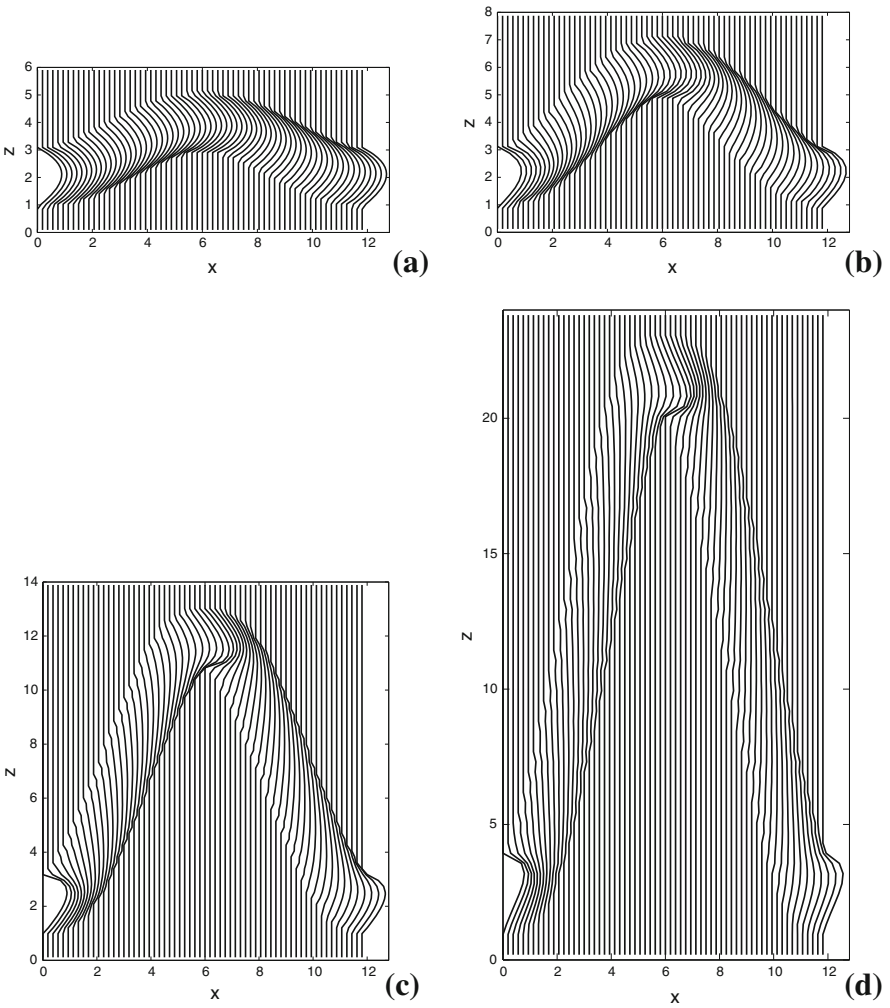

Fig. 9 Profiles of the streamwise velocity component u at $Re = 1$. Parameters as in Fig. 8

$C = 2$. We observe a clear convergence in the pressure evolution by comparing results obtained upon doubling the resolution several times. At $Re = 1$ and $Re = 100$ we quite closely recover first order convergence. In fact, we consider the convergence ratio $q = ((\Delta p)_{2N} - (\Delta p)_N)/((\Delta p)_{4N} - (\Delta p)_{2N})$ for the three finest grids with number of grid points N, $2N$ and $4N$. At $Re = 1$ we find at $t = 0.05$; $q = 2.4$ and at $Re = 100$ and $t = 5$; $q = 1.8$. Both are quite close to the values that would imply first order convergence. The flow at both Reynolds numbers approaches a steady state.

3.3 Flow in model aneurysm

In this subsection we present the velocity vector field and pressure differences for the flow inside the model aneurysm. The simulations are performed at Reynolds

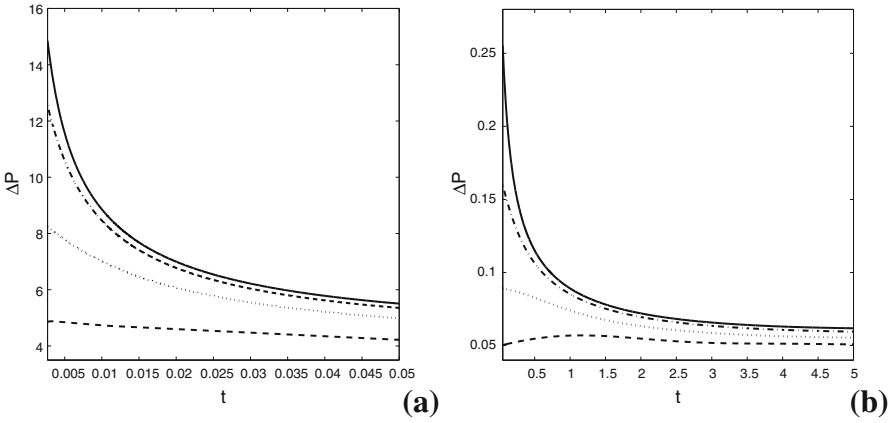

Fig. 10 Convergence of the IB method for flow inside a curved cylindrical vessel, at curve-parameter $C = 2$ in terms of the evolution of the pressure difference over the streamwise extent as a function of time. Simulations are done at $Re = 1$ (**a**), $Re = 100$ (**b**) at several grid resolutions: $32 \times 8 \times 16$ (*dash*), $64 \times 16 \times 32$ (*dot*), $128 \times 32 \times 64$ (*dash-dot*) and $256 \times 64 \times 128$ (*solid*). With increasing resolution the numerically obtained solution is seen to converge to a grid independent result

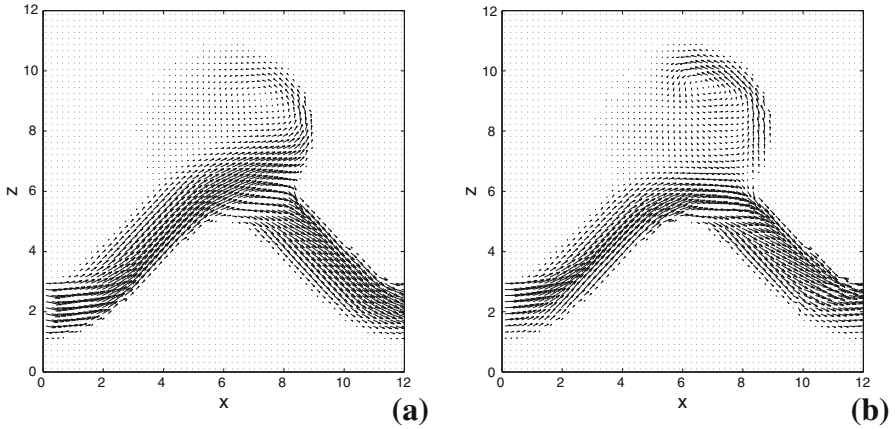

Fig. 11 Snapshot of the developing flow inside a model aneurysm at $Re = 100$ (**a**) and $Re = 250$. The flow is visualized in a cross section through the geometry, by plotting the in-plane velocity vectors. Results are shown for grid resolution $64 \times 32 \times 64$

numbers $Re = 100$ and $Re = 250$. The velocity field distributions inside these model aneurysms are presented in Fig. 11. Previously, we showed the flow in a curved vessel, which is laminar and steady at both Reynolds numbers. The addition of an aneurysm cavity renders the flow slightly unsteady at $Re = 250$. Some vortical flow structures are seen inside the aneurysm. We observe quite similar flow patterns albeit with more pronounced vortices inside the flow field at $Re = 250$.

In Fig. 12 we consider the pressure drop required to maintain the flows at $Re = 100$ (Fig. 12a) and $Re = 250$ (Fig. 12b) through the model aneurysm. At $Re = 250$ the result appears to indicate first signs of sustained unsteadiness while the solutions at

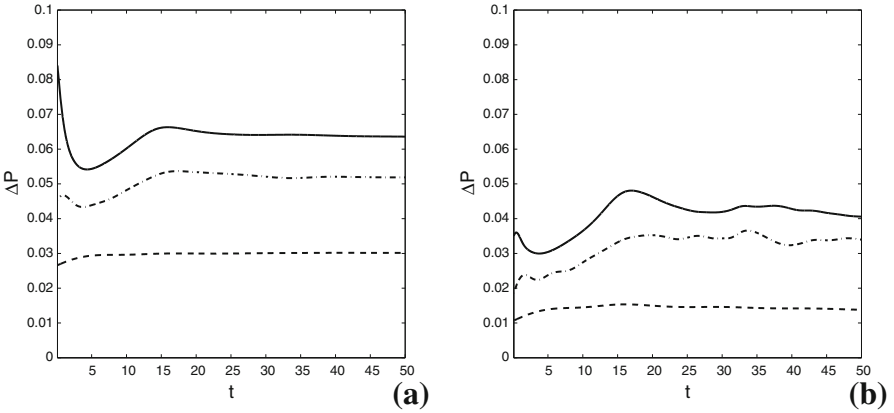

Fig. 12 Convergence of the IB method for flow inside a model aneurysm in terms of the evolution of the pressure difference over the streamwise extent as a function of time. Simulations are done at $Re = 100$ (**a**) and $Re = 250$ (**b**) at several grid resolutions: $16 \times 8 \times 16$ (*dash*), $32 \times 16 \times 32$ (*dash-dot*) and $64 \times 32 \times 64$ (*solid*)

$Re = 100$ becomes steady after some time. For this case only three refinements were included in view of computational time. With increasing grid resolution the computed flow converges for both flow regimes, roughly expressing the first order convergence shown previously for Poiseuille flow. The convergence rate q was also computed for both Reynolds numbers and it takes values $q = 1.86$ at $Re = 100$ and $q = 3.05$ at $Re = 250$ at $t = 50$.

4 Shear stress in curved vessel and model aneurysm

In this section we focus on the shear stress which develops inside the flow domain and at the vessel walls as a result of the blood flow inside. We first illustrate the IB approach for the shear stress associated with Poiseuille flow in a straight cylindrical pipe. This extends the validation study shown in the previous section by establishing the accuracy with which also the gradient of the velocity can be obtained numerically. Subsequently, we apply our method to compute shear stress in a curved 'sinusoidal' vessel and in a model aneurysm.

4.1 Validation of the IB computed shear stress

The main challenge for any IB method is to capture the flow near solid-fluid interfaces. In this region the highest velocity gradients may occur, leading to correspondingly highest levels of numerical error. During the initiating stages of an aneurysm, local high pressure and shear stresses may contribute to the growth, while in developed stages low shear stress levels may contribute to degenerative changes (Shojima et al. 2004; Boussel et al. 2008). This makes the shear stress, in particular regions of low shear stress, a quantity of relevance for understanding the often slow growth of an aneurysm (Castro et al. 2009), as well as a key component in mechanisms involved in sometimes much more rapid aneurysm development (Doenitz et al. 2010).

In the sequel we define the shear stress and clarify the method with which it was extracted from the numerical solution.

We define the shear stress in terms of the gradient of the velocity as follows. The rate-of-strain tensor S is given by

$$S = \frac{1}{2}(\nabla \mathbf{u} + \nabla \mathbf{u}^T) \tag{13}$$

The shear stress τ is a measure for the gradient of the velocity and we formulate it in terms of the components of S as follows:

$$\tau \equiv \frac{1}{Re}\sqrt{2S : S} \tag{14}$$

The normal stresses are contained on the diagonal elements of the tensor S and the tangential (shear) stresses are defined by the off-diagonal elements of S (Pope 2003). As point of reference for our numerical approach, we compute analytically the shear stress that results from (14) for the classical cases of a channel flow and a pipe flow. We obtain from (14)

$$\tau = \frac{1}{Re}\left|\frac{\partial u}{\partial y}\right| \tag{15}$$

for channel flow (in Cartesian coordinates) and for pipe flow in cylindrical coordinates (Young et al. 1997). This demonstrates that (14) is a convenient form of expressing the shear stress for more general cases.

In Sect. 3 we discussed laminar Poiseuille flow showing parabolic velocity profiles. Here, we extend this validation to shear stress, and expect linear profiles for τ. Within velocity field $(u, v, w) = (1 - r^2, 0, 0)$ we find $S : S = 2r^2$ and hence obtain

$$\tau = \frac{2}{Re}|r| \tag{16}$$

We validate the shear stresses for steady flow at $Re = 250$ and compare numerical solutions for the three masking strategies with the analytical result in (16).

Profiles of the shear stress distribution inside the cylindrical tube are collected in Fig. 13. The solid line is the analytical result for the cylindrical tube. With increasing grid resolution the numerical solution is seen to converge to the analytical shear stress. To assess the order of convergence we computed the difference in L_2 norm (see Fig. 14). We observe that the convergence of the shear stress is similar to that of the velocity predictions. For the 'outer' strategy the convergence appears somewhat slower than for the 'inner' and 'basic' methods. The resolution beyond which first order convergence is quite established appears to be higher than was required for the velocity predictions (Fig. 7a).

The first order convergence of the shear stress, i.e., the derivative of the velocity, on the basis of a numerical solution for the velocity that itself converges to first order may

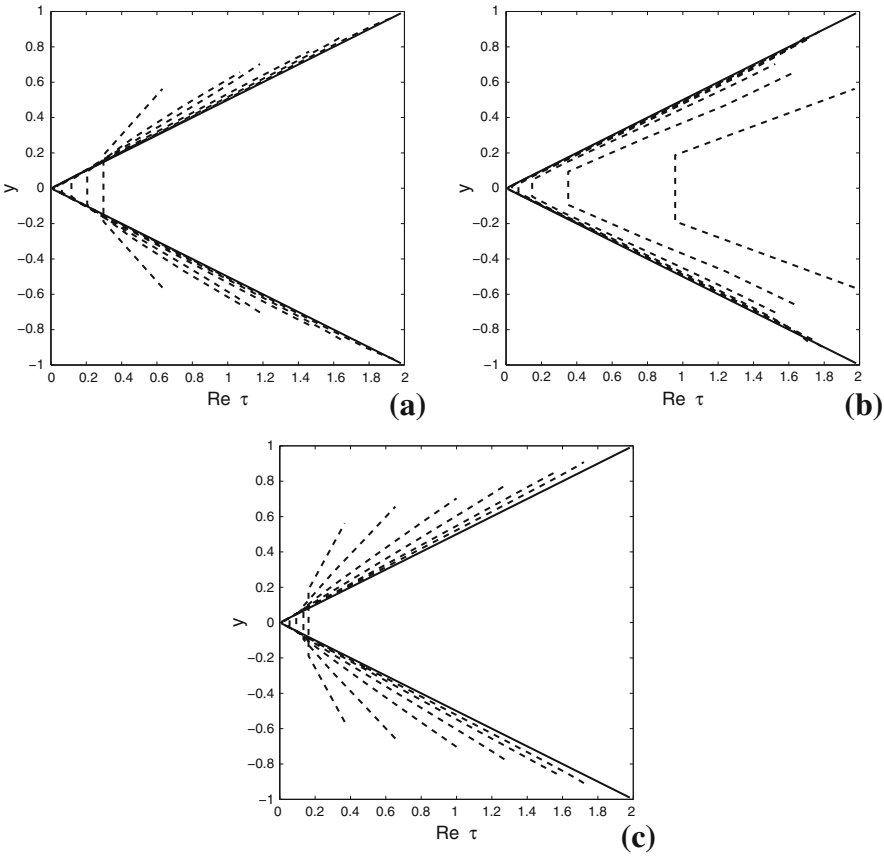

Fig. 13 Shear stress profiles for Poiseuille flow in a cylindrical tube for 'basic' (**a**), 'inner' (**b**) and 'outer' (**c**) masking strategies. Numerical solutions (*dashed lines*) converge to the exact solution (*solid line*) with increasing grid resolution. Shear stress profiles are obtained for a number of different grid resolutions $4 \times N \times N$ with $N = 8, 16, \ldots, 256$. Simulations are done for laminar flow at $Re = 250$

appear somewhat surprising. However, an argument why such first-order convergence for the derivative should arise can briefly be sketched as follows. We use a 1d setting for convenience and denote the approximation of the solution U in the point x_j by u_j. Assuming first-order convergence implies

$$u_j = U(x_j) + a_j h + \ldots \tag{17}$$

where a_j denotes the coefficient for the first order error term and h denotes the grid spacing. Using a simple discretization δ_x for the first derivative, this implies

$$\begin{aligned} \delta_x u_j \equiv \frac{1}{h}(u_{j+1} - u_j) &= \left\{ \frac{1}{h}(U(x_{j+1}) - U(x_j)) \right\} + (a_{j+1} - a_j) + \ldots \\ &= \left\{ U'(x_j) + O(h) \right\} + (a_{j+1} - a_j) + \ldots \end{aligned} \tag{18}$$

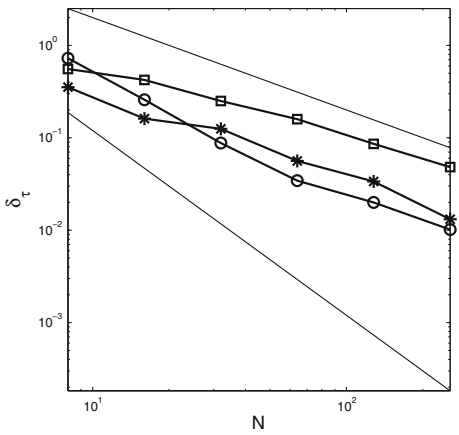

Fig. 14 Convergence of shear stress for Poiseuille flow measured in terms of the discrete L_2 norm δ_τ. *Solid lines* without markers denote slopes -1 and -2 respectively. The line marked with *circles* corresponds to the 'inner' strategy, the line with *asterisks* is for the 'basic' strategy, the line with *squares* is for the 'outer' strategy for generating the masking function

The term between brackets in (18) contains the exact derivative $U'(x_j)$ and a first order correction $O(h)$ associated with the use of the simple finite differencing δ_x to approximate the derivate. In addition, a term $a_{j+1} - a_j$ appears from the error term in the approximation of the solution. This term seems to imply 'zero-order', i.e., no convergence of the numerical derivative. However, if the error term is differentiable, i.e., if we assume $a_{j+1} = a_j + a'_j h + \ldots$ we obtain first-order convergence of the derivative, also if the accuracy with which the solution itself is approximated is of first order. For the Poiseuille case, the (slow) first order convergence as illustrated in Fig. 14 appears to underpin the differentiability of the error term.

4.2 Analysis of the shear stress distribution inside curved vessel and model aneurysm

In this subsection we consider shear stresses in a curved vessel and a model aneurysm. We present the distribution of the shear stress first in two-dimensional cross sections of both geometries and later focus on the 1d shear stress profiles.

In Fig. 15 the distribution of the shear stress is shown as a contour plot on a two-dimensional cross section along the middle plane inside both geometries. We normalize the shear stress field by its maximum value to emphasize the main patterns. High shear stress values are represented as dark areas. We observe that inside the aneurysm cavity a detached jet forms, which impinges on the wall to create a region of locally intensified shear stress. The shear stress τ is also quite large near 'extremities' of the curved cylindrical tube that is connected to the sphere. At the higher Reynolds number $Re = 250$ the results are qualitatively similar to the ones at $Re = 100$. In case of the spherical aneurysm we observe a significant separated vortex which dominates the stress distribution on the cavity wall (Fig. 15b).

To consider the accuracy with which τ is predicted in more details, we perform a grid-refinement study and present 1d shear stress profiles. In Fig. 16a characteristic stress profile is presented as function of z taken at $(x, y) = (L_x/2, L_y/2)$ at various resolutions. We plot the quantity $(Re\ \tau)$ in order to compare the convergence of the shear stress quite independently of flow conditions.

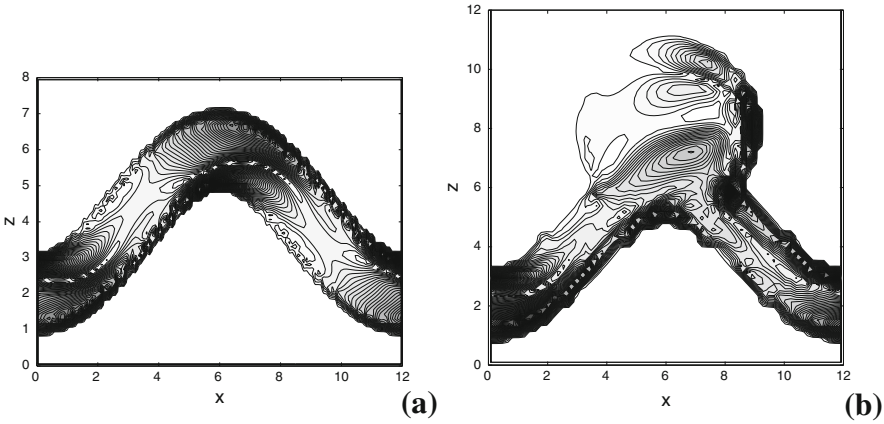

Fig. 15 Cross-sectional slices of the normalized shear-stress distribution inside a curved vessel (**a**) and a model aneurysm (**b**). The shear stress at $Re = 100$ is shown. High shear stress values are found near the walls of the vessel and near the rims of the attached spherical cavity (*dark areas*). The spatial resolution that was adopted is $128 \times 32 \times 64$ for the curved vessel (**a**) and $64 \times 32 \times 64$ for the model aneurysm (**b**)

For each model geometry at both Reynolds numbers $Re = 100$ and $Re = 250$ we notice better capturing of the shear stress profile with increasing grid resolution. Due to the computational time the shear profiles for the model aneurysm are collected at lower resolution (along x-axis) than for the curved vessel. Inside both geometries we observe a complex spatial dependence with peaks near the walls. The value $(Re\ \tau)$ stays approximately the same when the Reynolds number changes in the steady flow regime. This means that with increasing Reynolds number, the shear stress τ decreases, as was also seen for Poiseuille flow in (16). We also notice that in the curved vessel the maximum value of the shear stress is about twice as high compared to the model aneurysm. This suggests that having an aneurysm leads to a decrease in the local shear stresses inside the vessel; relocating local maxima partially into the aneurysm body. This was also observed by (Shojima et al. 2004) who reported average wall-shear stress levels about a factor of two lower in the aneurysm than in the nearby vessel region. Although convergence is not complete with our current method, at the resolutions studied, we obtain a reliable impression of τ throughout the domain. Further refinement of the grid was not practical at the adopted Reynolds numbers with the current single-cpu implementation of the simulation software. In order to simulate long enough until satisfactorily reaching the steady state at $Re = 250$, we face computing times on the order of 100 hours on a modern cpu for a single geometry. Since we employ explicit time-stepping, an increase in resolution by a factor of 2 in each direction, would increase the computing time by a factor of about 16, making the endeavor unfeasible. Current efforts are in the direction of parallel implementation of the flow solver. Linking to existing literature, we can further underpin the reliability of the predictions. The work reported by Tseng and Ferziger (2003) showed that IB methods are capable of capturing shear stresses throughout the domain with an accuracy that is comparable to that of conventional body-fitted finite-volume discretizations. This puts the results in Fig. 16 into perspective.

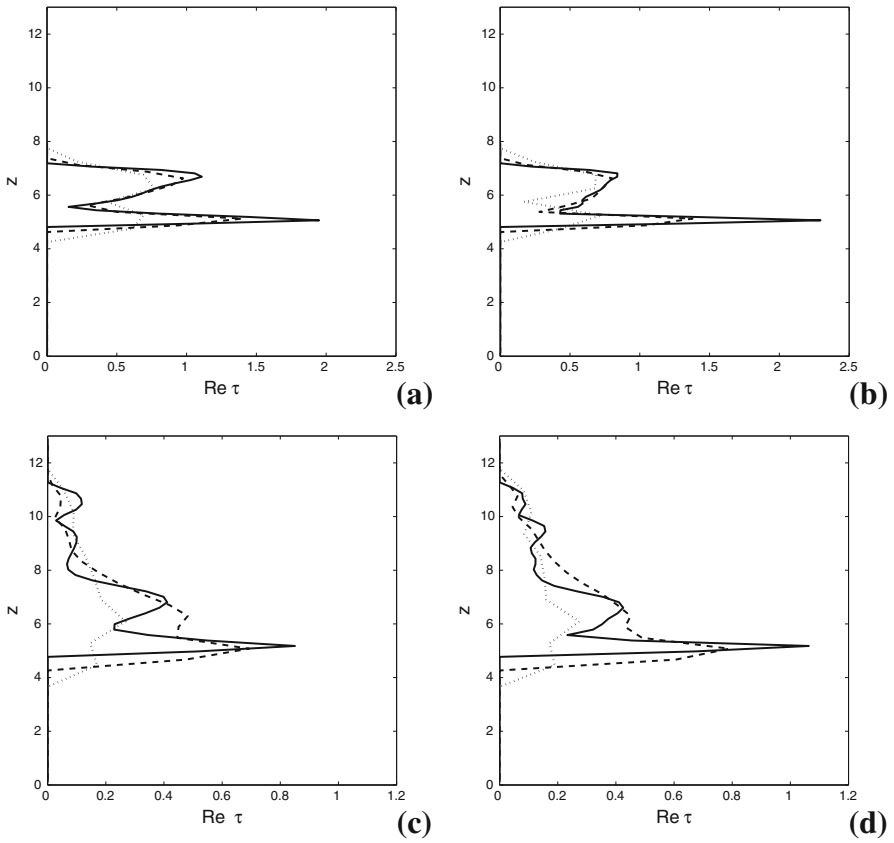

Fig. 16 Shear stress profiles in a curved vessel (**a**, **b**) and a model aneurysm (**c**, **d**). At $Re = 100$ (**a**, **c**) and $Re = 250$ (**b**, **d**) we show the shear stress profile at different grid resolutions: curved vessel grid resolutions: $32 \times 8 \times 16$ (*dot*), $64 \times 16 \times 32$ (*dash*) and $128 \times 32 \times 64$ (*solid*), model aneurysm grid resolutions: $16 \times 8 \times 16$ (*dot*), $32 \times 16 \times 32$ (*dash*) and $64 \times 32 \times 64$ (*solid*). For the curved vessel (model aneurysm) we use as domain $[L_x, L_y, L_z] = [12, 4, 8]([12, 8, 13])$. Hence, the grid spacings for both cases differs, although the number of grid points is equal

In Poiseuille flow we established first-order convergence of the shear stress, including the value at the wall, with our method (cf. Fig. 13). We expect this level of convergence to be maintained also in case of smoothly curved vessels and the model aneurysms, although a strict underpinning with numerical results was not provided in view of the limitations in the spatial resolution that could be employed.

5 Concluding remarks

In this paper we presented a basic immersed boundary (IB) method and its application to the simulation of blood flow in models for cerebral aneurysms. We first described the medical condition and possible ways of diagnostics and treatment of

aneurysms. This motivates how mathematical modeling might be applied for surgical support. We introduced a computational model, based on the incompressible Navier–Stokes equations, in which an additional forcing term determines the complex geometry in our IB method. The masking function assigns to every grid cell the property 'fluid' or 'solid'. Based on the property in the center of a cell, or associated with the corner points, we arrive at three slightly different strategies, called 'basic', 'inner' and 'outer', to define complex-shaped fluid domains. On a 3D Cartesian grid, for any non-aligned geometry we obtain a staircase representation of the fluid-solid boundaries.

The IB method as developed here offers the potential of a more direct computational chain from the raw, somewhat coarse biomedical imagery of cerebral vasculature to a CFD analysis of the flow and shear stresses. In conventional body-fitted methods a time-consuming process of segmentation has to be incorporated in order to prepare the rough data for such a computational analysis. The IB approach could be less user-intensive and offer the opportunity to develop an automated analysis of the haemodynamics in diseased areas.

A detailed validation analysis of the IB method was provided for Poiseuille flow in a tube with a circular cross section, showing first order global convergence of the numerical solution as well as of its gradients. In particular, we showed the influence of the masking function strategies on the level of accuracy of the numerical flow solution. Based on the validation analysis we choose the 'basic' masking strategy for further simulations.

We applied our method to different geometries, motivated by medical conditions. We included a curved vessels and a model aneurysm. The curved vessel is a cylindrical tube with a sinusoidal centerline, while the model aneurysm is simplified to a sphere merged with the curved vessel. For these geometries we computed velocity fields to understand the behavior of the flow. For different Reynolds numbers we presented a grid refinement study for some flow characteristics and showed convergence of the method.

We also presented shear stresses, as these are often associated with possible rupture of aneurysms either directly or as indicator of the flow structure. The shear stress distribution in curved vessels and model aneurysms was discussed on different levels: general, 2d cross-section and 1d profiles to quantify the results. We observed the locations of higher shear stresses near the walls as well as near the region where the neck of the aneurysm where it is connected to the vessel. We noticed that the presence of an aneurysm causes the shear stress levels to be reduced, compared to the situation without spherical cavity. This is in line with findings reported by (Shojima et al. 2004), who reported a reduction by a factor of two in the average shear stress in the aneurysm, compared to the flow in the connecting vessels. Moreover, we noticed that the peak values of the shear stress are relocated into the aneurysm cavity. Ongoing work deals with the application of the IB method described in this paper to realistic geometries and realistic pulsatile flows, which are obtained from real medical data. This will be presented elsewhere.

Acknowledgments The authors gratefully acknowledge NCF support through project SH061, for computations at the Huygens computer at SARA.

References

Angot P, Bruneau CH, Frabrie P (1999) A penalization method to take into account obstacles in viscous flows. Numer Math 81:497–520

Arthurs KM, Moore LC, Peskin CS, Pitman EB, Layton HE (1998) Modeling arteriolar flow and mass transfer using the immersed boundary method. J Comput Phys 147:402–440

Batchelor GK (2007) An introduction to fluid dynamics. Cambridge University Press, Cambridge

Bernsdorf J, Wang D (2009) Non-Newtonian blood flow simulation in cerebral aneurysms. Comp Math Appl 58:1024–1029

Berthelsen PA, Faltinsen OM (2008) A local directional ghost cell approach for incompressible viscous flow problems with irregular boundaries. J Comput Phys 227(9):4354–4397

Boussel L, Rayz V, McCulloch C, Martin A, Acevedo-Bolton G, Lawton M, Higashida R, Smith WS, Young WL, Saloner D (2008) Aneurysm growth occurs at region of low wall shear stress: Patient-specific correlation of hemodynamics and growth in a longitudinal study. Stroke 39:29973002

Castro MA, Putman CM, Sheridan MJ, Cebral JR (2009) Hemodynamic patterns of anterior communicating artery aneurysms: a possible association with rupture. Am J Neuroradiol 30:297–302

Cebral JR, Castro MA, Burgess JE, Pergolizzi RS, Sheridan MJ, Putman CM (2005a) Characterization of cerebral aneurysms for assessing risk of rupture by using patient-specific computational hemodynamics models. Am J Neuroradiol 26:2550–2559

Cebral JR, Castro MA, Appanaboyina S, Putman CM, Millan D, Frangi AF (2005b) Efficient pipeline for image-based patient-specific analysis of cerebral aneurysms hemodynamics: technique and sensitivity. IEEE Trans Med Imaging 24:457–467

Cheny Y, Botella O (2010) The LS-STAG method: a new immersed boundary/level-set method for the computation of incompressible viscous flows in complex moving geometries with good conservation properties. J Comput Phys 229(4):1043–1076

Cortez R, Fauci L, Cowen N, Dillon R (2004) Simulation of swimming organisms: coupling internal mechanics with external fluid dynamics. Comput Sci Eng 6:38–45

Dillon R, Fauci L, Fogelson A, Gaver D III (1996) Modeling biofilm processes using the immersed boundary method. J Comput Phys 129:57–73

Doenitz C, Schebesch KM, Zoephel R, Brawanski A (2010) A mechanism for the rapid development of intracranial aneurysms: a case study. Neurosurgery 67(5):1213–1221

Gambaruto AM, Janela J, Moura A, Sequeira A (2011) Sensitivity of hemodynamics in a patient specific cerebral aneurysm to vascular geometry and blood rheology. Math Biosci Eng 8(2):409–423. doi:10.3934/mbe.2011.8.409

Gao T, Tseng YH, Lu XY (2007) An improved hybrid Cartesian/immersed boundary method for fuid-solid flows. Int J Numer Meth Fluids 55(12):1189–1211

Geurts BJ (2003) Elements of direct and large-Eddy simulation. Edwards Publishing. ISBN: 1-930217-07-2

Gijsen FJH, van de Vosse FN, Janssen JD (1999) The influence of the non-Newtonian properties of blood on the flow in large arteries: steady flow in a carotid bifurcation model. J Biomech 32:601–608

Griffith BE, Peskin CS (2005) On the order of accuracy of the immersed boundary method: higher order convergence rates for sufficiently smooth problems. J Comput Phys 208:75–105

Hendrikse J, van Raamt AF, van der Graaf Y, Mali WPTM, van der Grond J (2005) Distribution of cerebral blood flow in the circle of Willis. Radiology 235:184–189

Hirsch C (1988) Numerical computation of internal and external flows. Wiley, New York

Iaccarino G, Verzicco R (2003) Immersed boundary technique for turbulent flow simulations. Appl Mech Rev, ASME 56(3):331–347

Janela J, Moura A, Sequeira A (2010) A 3D non-Newtonian fluid-structure interaction model for blood flow in arteries. J Comput Appl Math 234:2783–2791

Kamath S (1981) Observations on the length and diameter of vessels forming the circle of willis. J Anat 133:419–423

Kang S, Iaccarino G, Ham G, Moin P (2009) Prediction of wall-pressure fluctuation in turbulent flows with an immersed boundary method. J Comput Phys 228(18):6753–6772

Keetels GH, DOrtona U, Kramer W, Clercx HJH, Schneider K, van Heijst GJF (2007) Fourier spectral and wavelet solvers for the incompressible NavierStokes equations with volume-penalization: convergence of a dipolewall collision. J Comput Phys 227:919–945

Khadra K, Angot P, Parneix S, Caltagirone JP (2000) Fictitious domain approach for numerical modelling of Navier–Stokes equations. Int J for Num Meth in Fluids 34:651–684

Kim Y, Peskin CS (2006) 2-D parachute simulation by the immersed boundary method. SIAM J Sci Comput 28(6):2294–2312

Koffijberg H, Buskens E, Algra A, Wermer MJH, Rinkel GJE (2008) Growth rates of intracranial aneurysms: exploring constancy. J Neurosurg 109:176–185

Kovalev K (2005) Unstructured hexahedral non-conformal mesh generation. Dissertation, Vrije University of Brussels, Brussels

Ku DN (1997) Blood flow in arteries. Annu Rev Fluid Mech 29:399–434

Lai MC, Peskin CS (2000) An immersed boundary method with formal second-order accuracy and reduced numerical viscosity. J Comput Phys 160:705–719

Li Y, Yun A, Kim J (2011) An immersed boundary method for simulating a single axisymmetric cell growth and division. J Math Biol. doi:10.1007/s00285-011-0476-7

Liu Q, Vasilyev OV (2007) A Brinkman penalization method for compressible flows in complex geometries. J Comput Phys 227:946–966

Löhner R, Baum JD, Mestreau EL, Rice D (2007) Comparison of body-fitted, embedded and immersed 3-d euler predictions for blast loads on columns. Am Inst Aeronaut Astrounat paper, pp 1–22

Lopez Penha DJ, Geurts BJ, Stolz S, Nordlund M (2011) Computing the apparent permeability of an array of staggered square rods using volume-penalization. Comput Fluids 51:157–173

Mikhal J, Geurts BJ (2011) Bounding solutions for cerebral aneurysms. New Arch Math 5/12(3):163–168

Mittal R, Iaccarino G (2005) Immersed boundary methods. Annu Rev Fluid Mech 37:239–261

Moret J, Kemkers R, Op de Beek J, Koppe R, Klotz E, Grass M (1998) 3D rotational angiography: clinical value in endovascular treatment. Medicamundi 42(3):8–14

Mori Y (2008) Convergence proof of the velocity field for a Stokes flow immersed boundary method. Comm Pure and Appl Math LXI:1213–1263

Oubel E, De Craene M, Putman CM, Cebral JR, Frangi AF (2007) Analysis of intracranial aneurysm wall motion and its effects on hemodynamic patterns. In: Hu XP (ed) SPIE medical imaging 2007: physiology, function, and structure from medical images, vol 6511, Manduca A. SPIE Press, San Diego, pp 10–11

Oubel E, Cebral JR, De Craene M, Blanc R, Blasco J, Macho J, Putman CM, Frangi AF (2010) Wall motion estimation in intracranial aneurysms. Physiol Meas 31:1119–1135

Perktold K, Peter R, Resch M (1989) Pulsatile non-Newtonian blood flow simulation through a bifurcation with an aneurysm. Biorheol 26(6):1011–1030

Peskin CS (2002) The immersed boundary method. Acta Numeric. doi:10.1017/s0962492902000077

Pope SB (2003) Turbulent flows. Cambridge University Press, Cambridge

Quarteroni A, Formaggia L (2004) Mathematical modelling and numerical simulation of the cardiovascular system. In: Ciarlet PG, Lions JL (eds) Handbook of numerical analysis, vol 12. North-Holland, Amsterdam, pp 3–127

Sarthou A, Vincent S, Caltagirone JP, Angot P (2007) Eulerian–Lagrangian grid coupling and penalty methods for the simulation of multiphase flows interacting with complex objects. Int J Numer Meth Fluids 56:1093–1099. doi:10.1002/fld.1661

Seo JH, Mittal R (2011) A high-order immersed boundary method for acoustic wave scattering and low-Mach number flow-induced sound in complex geometries. J Comput Phys 230:1000–1019

Shashkov M, Steinberg S (1995) Support-operator finite-difference algorithms for general elliptic problems. J Comput Phys 118:131–151

Shojima M, Oshima M, Takagi K, Torii R, Hayakawa M, Katada K, Morita A, Kirino T (2004) Magnitude and role of wall shear stress on cerebral aneurysm computational fluid dynamic study of 20 middle cerebral artery aneurysms. Stroke 35:2500–2505

Sprengers ME, Schaafsma J, van Rooij WJ, Sluzewski M, Rinkel GJE, Velthuis BK, van Rijn JC, Majoie CB (2008) Stability of intracranial aneurysms adequately occluded 6 months after coiling: a 3T MR angiography multicenter long-term follow-up study. Am J Neuroradiol 29:1768–1774

Tseng YH, Ferziger JH (2003) A ghost-cell immersed boundary method for flow in complex geometry. J Comput Phys 192:593–623

van Rooij WJ, Sprengers ME, Sluzewski M, Beute GN (2007) Intracranial aneurysms that repeatedly reopen over time after coiling: imaging characteristics and treatment outcome. Neuroradiol 49:343–349

van Rooij WJ, Sprengers ME, de Gast AN, Peluso APP, Sluzewski M (2008) 3D rotational angiography: the new gold standard in the detection of additional intracranial aneurysms. Am J Neuroradiol 29:976–979

Vasilyev OV, Kevlahan NKR (2002) Hybrid wavelet collocationBrinkman penalization method for complex geometry flows. Int J Numer Meth Fluids 40:531–538

Verstappen RWCP, Veldman AEP (2003) Symmetry-preserving discretization of turbulent flow. J Comput Phys 187:343–368

Wiebers DO, Whisnant JP, Forbes G et al (1998) Unruptured intracranial aneurysms—risk of rupture and risks of surgical intervention. International study of unruptured intracranial aneurysms investigators. New England J Med 339(24):1725–1733

Young DF, Munson BR, Okiishi TH (1997) A brief introduction to fluid mechanics. Wiley, New York